

Method for Remote Sensing Oil Spill Applications Over Thermal and Polarimetric Imagery

Thaweesak Trongtirakul , Sos Agaian , *Fellow, IEEE*, Adel Oulefki , and Karen Panetta , *Fellow, IEEE*

Abstract—Several oil spill disasters have been reported in the last decade, posing a major threat to the marine ecosystem, damaging marine life, vital for protecting the environment, and reducing economic losses. In order to reduce or clean the oil spill, one needs to create a cost-effective oil spill detection system, including its source, the spill extent, the quantity estimate, the range of probable transport paths, and weather and sea conditions. Thermal and polarimetric imagery are emerging sensing modalities that show the potential for enhanced contrast in situations where conventional imaging, such as microwave, hyper-spectral, and visible imaging, has recently been researched. There is a need to compare existing thermal and polarimetric images since there is little work and data in this area. Current studies have shown some improvement in oil spill technique development. Even with the additional availability of new techniques, these steps are limited by cloud cover and lack of contrast. This article will investigate thermal and polarimetric cameras' usage for tracking 3-D oil spills in the sea by developing robust unsupervised oil sensing algorithms. It involves introducing: 1) an oil spill segmentation framework designed for thermal and polarimetric imagery; 2) a multidensity oil spill region enhancement and 3-D thickness visualization algorithm; and 3) a qualitative and quantitative oil spill analysis approach. Comparisons with existing algorithms demonstrate the effectiveness of the proposed algorithms.

Index Terms—Oil density detection, oil spill, polarimetric image, polarization, thermal imagery.

I. INTRODUCTION

THE oceans cover approximately (71%) of the total surface area of Earth and are an essential component of Earth's ecosystem [1], [2]. With increased maritime traffic, sudden oil spill disasters have become more common [3], [4], [5]. Similarly, floating crude oil on ocean surfaces can harm marine and coastal environments and fisheries [6]. According to the European Space Agency (ESA), over five million tons of oil are spilled each

year, with at least (45%) of that due to operational discharges from ships. Furthermore, oil spills are significant incidents that have long-term consequences for the maritime environment [7]. Furthermore, oil spill disaster management, such as the Mauritius oil spill in 2020, which spilled 1200 tons of oil into the ocean, has far-reaching and long-term consequences. The oil may float on the sea surface for days or months, changing its chemical composition due to weathering. Oil spill detection aims to identify dark spots in images at any time, which is difficult because the scattering areas associated with oil spills are subject to change due to water surface movement. Sensing oil spill data is critical for a variety of reasons, including oil spill mapping for tactical and strategic countermeasures; gathering legal evidence; law enforcement, including ship discharge monitoring; direct support for oil spill countermeasures; and determining slick trajectory [8]. It should come as no surprise that spilled oil causes hydrocarbon pollution, which is toxic to all living things. Given the importance of acquiring data on oil spills for proactive intervention and pollution reduction in the environment and ecosystems [9], this step necessitates additional information regarding the slick's location, type, size, and thickness [3]. However, significant progresses have been made using cameras in visible and infrared spectra. However, many critical data issues remain unexplored because oil has no distinct spectral information that distinguishes it from the water in which it floats [10]. Furthermore, [11] supports this interpretation by stating that technologies used to detect oil slicks range from laser floor sensors to microwave sensors via optical remote sensing (ultraviolet and others).

In practice, the most widely used and low-cost method uses infrared sensors to some extent for optical remote sensing. This article will demonstrate the various types of thermal infrared sensors were used to determine their potential for measuring oil film and identifying fuel. Oil spill monitoring technology using infrared wavelengths, on the other hand, has grown in popularity because it is widely accepted, portable, low-cost, and easy to use [12]. It correctly detects the thickness of an oil spill by detecting thermal infrared emissivity, as indicated in [13]. Furthermore, the authors make use of spectral emissivity's multicollinearity. The thermal infrared emissivity properties of oil films can be summarized as follows: 1) the emissivity changes dramatically when the films are thin; 2) the emissivity varies as oil film thickness increases; and 3) thermal imaging information shows blurred boundaries between the oil film region and a water surface.

Manuscript received 8 July 2022; revised 2 November 2022 and 13 January 2023; accepted 22 January 2023. Date of publication 8 May 2023; date of current version 14 July 2023. (Thaweesak Trongtirakul, Sos Agaian, and Karen Panetta contributed equally to this work.) (Corresponding author: Adel Oulefki.)

Associate Editor: M. Haller.

Thaweesak Trongtirakul is with Rajamangala University, Bangkok 10300, Thailand (e-mail: thaweesak.tr@rmutp.ac.th).

Sos Agaian is with the Graduate Center, City University of New York, New York, NY 10314 USA (e-mail: sos.agaian@csi.cuny.edu).

Adel Oulefki is with the CDTA Research Center, Algiers 16018, Algeria (e-mail: adel.oulefki@fulbrightmail.org).

Karen Panetta is with Tufts University, Medford, MA 02155 USA (e-mail: karen@eecs.tufts.edu).

Digital Object Identifier 10.1109/JOE.2023.3245759

TABLE I
COMPARISON OF CONVENTIONAL THERMAL IMAGERY AGAINST POLARIMETRIC IMAGERY

Descriptions	Thermal	Polarimetric
Commercial Cost [36]	High	More expensive
Image quality	Relies on [8]: <ul style="list-style-type: none"> • Focus of an infrared sensor • Optics of a thermal imagery • Spatial resolution (pixels + field of view) 	Relies on [16]: <ul style="list-style-type: none"> • Rotating element of division of time • Division of amplitude and aperture
Color content information	<ul style="list-style-type: none"> • Raw: gray-scale [14] • Enhanced: color by a color-map 	<ul style="list-style-type: none"> • Raw: gray-scale [37] • Enhanced: color by a color-map
Record image through translucent obstacles [33]	Yes	Yes
Visibility in low or no light [33]	Yes	Yes
Distinguish objects at varying distances [38]	No	No
Display surface temperatures of solid objects [38]	Yes	Yes
Display surface temperatures of water [16]	Yes	Yes
Presence of noise [38]	Low – Medium	Low – Medium
Existing tools for a solid segmentation [10]	Limited	Limited
Consumer applications [38]	Limited	Limited
Advantages [10]	Reveals details inside regions	Provides strong regions
Disadvantages [10]	Blurred edges due to heat radiation	Fusing operators and angles of reflection

Optical polarization remote sensing, which has been used for decades, may provide a new solution for oil spill detection. The study shows that polarimetric sensors can extract more visual information from light polarization [14]. So, by having one or more polarimetric parameters [15], we can extract details from a scene that are not readily apparent when using conventional thermal imagers alone [16]. These measurements have the potential to provide polarization contrast due to material differences, which we are utilizing here for oil-on-water detection [16]. To distinguish an object from the background, the commonly used degree of linear polarization (DoLP) is oriented at 0° and 90° , and 45° and 135° (left-to-right and top-to-bottom). These measurements, however, required large scientific instruments that were not easily portable for handheld use in the past. The most recent advancements in uncooled infrared sensor arrays have resulted in a significant reduction in the size, weight, and cost of high-performance polarimetric sensors. Chenault et al. [16] demonstrated that polarimetric imaging can be an effective target detection tool in complex environments by analyzing the polarization property of the light emanating from the objects rather than the intensity [16]. Polarimetric imagery can be used to detect oil film [17], [18], [19]. For example, the authors in [18] and [20] conducted laboratory experiments to investigate the polarization properties of oil spills. Nonetheless,

their findings have yet to be validated on a satellite scale. Zhou et al. [21] detected oil spills in sun glints based on the degree of polarization using satellite images. However, only a few satellite images are used for validation. The quality of a DoLP image is determined by a number of important factors, as shown in Table I.

Fig. 1 depicts the imaging characteristics of thermal single-polarization and polarimetric images. Image segmentation and image enhancement techniques indicate regions with varying densities of oil films using different imaging properties. Furthermore, when compared to thermal imaging, the quality polarimetric image demonstrates firm boundaries between oil films and water surfaces, as shown in Fig. 1, marked as a shaded area for thermal and polarimetric imaging on the figure's top and bottom right.

The primary goal of accessing oil spillages is to accurately evaluate the oil film thickness, spill region, and spill density. Thermal and polarimetric imaging are commonly used in oil spill detection due to their unique abilities in nighttime searches and complex weather conditions. However, the commonly used radiation-based imagery is constrained by wind speed [19], [22]. It causes waves on the water's surface. As a result, the oil spill and seawater have a uniform contrast. According to some evidence, segmenting oil film regions into highly homogeneous

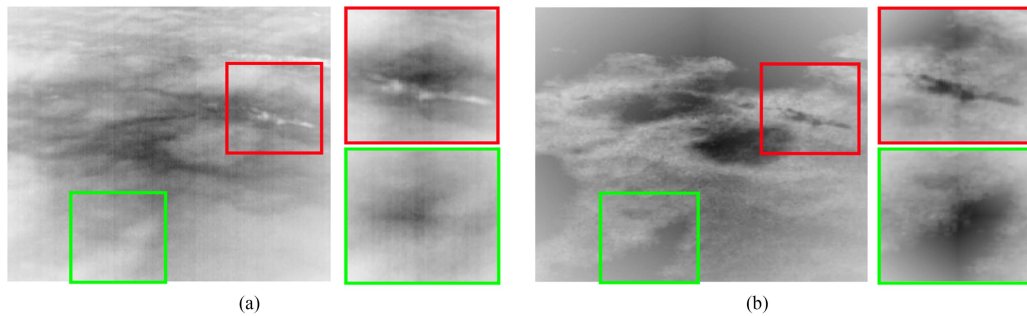


Fig. 1. Comparison of oil spill imaging (enlarged area size: 100×100). (a) Thermal image and (b) a polarimetric image. Thermal and polarimetric images reveal varying densities of oil films using different imaging properties. Polarimetric imaging outperforms thermal imaging in distinguishing firm boundaries between oil films and water surfaces.

regions is difficult. This calls into question the validity of both segmentation based on global thresholds. Following the standard procedure for oil spill detection, this process is divided into three stages—contrast enhancement, segmentation, and oil spill classification [10]. This research even includes contrast enhancement. Furthermore, the shortcomings of several commonly used methods must be addressed, including: 1) finding a versatile solution that can be applied to a large and constantly growing number of different regions of interest (ROI); 2) dealing with the vast variations in ROI properties; 3) dealing with the various oil spill image modalities [16]; 4) issues related to changes in signal homogeneity, primarily variability and noise for each object [14]. However, this study includes a detailed segmentation, which can be classified as manual, semiautomatic, or fully automatic [18]. The first category is time-consuming, monotonous, and can be influenced by intraobserver or interobserver variability. Semiautomatic methods are widely used and widely available. However, these techniques necessitate user-coarse initialization. Finally, fully automated procedures do not require user intervention. It necessitates the use of additional appropriate preprocessing algorithms, such as denoising, enhancements, and so on. Each of these approaches has advantages and disadvantages [23]. Our focus falls into this category because we strive for oil-spill segmentation and detection using unsupervised methods.

This article focuses on developing an automatic unsupervised oil spill detection approach using thermal and polarimetric images because: 1) the presented method does not require large data bases to train the algorithm parameters, which is critical for neural networks; 2) it is computationally cheap with an average 1.06 s only to run a sample image; and 3) it is simple to design, interpret, and use with low-power devices with limited memory, computational power, and power supply, which is sometimes more important (for example, for drone imaging and IoT). The following are the major contributions.

- 1) We propose an efficient method for multilevel thresholding using cross-entropy.
- 2) We develop an image drive-optimized enhancement algorithm for thermal and polarimetric images.
- 3) We develop a nature-inspired optimized multithreshold segmentation framework with 3-D visualization.

- 4) A comparison of the advantages and disadvantages of thermal and polarimetric image performance on the same oil spill data bases (the first work in this area).

The rest of this article is organized as follows. Section I provides a high-level overview of the research gap in oil spill segmentation. Section II elaborates on the research problem. The proposed oil spill segmentation for thermal and polarimetric images is described in Section III. Section IV illustrates and discusses the computer simulation results, and the final section summarizes the advantages of the proposed method over the state-of-the-art. Finally, Section V concludes this article.

II. BACKGROUND

This section will investigate the history of thermographic and polarimetric technologies. The conventional oil spill sensor approaches are compared in Table II. More detailed descriptions of the benefits and drawbacks of oil spill remote sensing are contained in [19]. We also examine the most commonly used image segmentation and binarization methods. Finally, we will demonstrate how binarization methods, both local and global, can be used to classify oil spills.

A. Polarimetric Imagery

In the 1990s, researchers began investigating oil spill detection using synthetic aperture radar sensors. Polarimetric images have gained popularity in the last decade. Prematurely, Solberg et al. [24] based oil spill detection (OSD) on texture analysis of single polarimetric images. They used a Bayesian classifier to extract (12) texture features from the dark spots of oil films. The polarimetric synthetic aperture radar sensors can acquire many details about the targets by measuring their complex scattering matrices, which is useful for analyzing and interpreting the scattering mechanism of oil slicks, look-alikes, and seawater, as well as realizing oil slick extraction and detection [25]. Polarimetric imaging is one of the most effective techniques for high-contrast imaging because it extracts visual information from light polarization [14]. Polarimetric imagery detection is a young and underdeveloped field [26]. The authors in [17] and [27] proved that polarimetric SAR imagery can be used for both spot oil slicks and distinguishing them from weak-damping

TABLE II
COMPARISON OF CONVENTIONAL OIL SPILL SENSOR IMAGERY APPROACHES [10]

Feature (Pros ✓ / Cons X)	Imaging methods				
	Laser	Polarimetric [34]	Visible	Thermal	Microwave (Radar)
Imaging Modes: Active/ Passive	✓	Hybrid	X	X	X
Coastal recording: Offshore/ Onshore	X	✓	✓	✓	✓
Image info: Day and Night/ Day only	✓	✓	X	✓	✓
Cost: Not expensive/expensive	X	X	✓	✓	X
Difficulty: Easy/ Difficult	X	✓	✓	✓	✓
Weather independent: Yes/No	X	✓	X	✓	✓
Spectral signature: Yes/No	X	✓	X	✓	✓

look-alikes of images captured under low-to-moderate wind conditions and at intermediate incidence angles. Remote sensing, computer sciences (object detection and classification), microscopic, planetary science, astronomy, military, surveillance, and weather radar applications are already using it. It is useful for distinguishing weak target signatures from their surroundings, as well as creating new images by fusing them with polarimetric or nonpolarimetric images.

B. Thermal Imagery

Not long ago, *IR* cameras were primarily used empirically for oil spill detection because they are low-cost, lightweight, and can detect oil spills at night. Recent studies have shown that 1) infrared sensors can detect oil films with (10–100 μ m) thickness; 2) the brightness of the infrared sensing-based imagery is low or during the cloud and heavy fog for good operation; 3) false-positive results can be obtained by misinterpreting the thermal radiation from seaweed; 4) oil spills can be detected using some thresholding techniques in the near infrared (NIR) spectrum (750–1000 nm), but this is prone to false negatives [28]; 5) crude oil has a different reflectance spectrum when compared to water in the short wave infrared band (1000–1700 nm) [29]; 6) oil spill detection using machine learning using a UAV *IR* image under controlled conditions and achieving 89% accuracy on a data set created during the experiment Thermal remote sensing detail reviews can also be found in [30] and [31].

C. Oil Spill Thermal and Polarimetric Imagery

The concept of thermographic sensors, first introduced in 1956, refers to radiation detection in the electromagnetic spectrum's long-infrared range. The amount of radiation emitted by a given object increases with temperature, warm objects stand out well against cooler backgrounds, which become easily visible day or night. Because it can provide spilling information during the day/night and work in adverse weather conditions, this technology enables us to detect oil spills and disaster management projects [10]. Despite this, the image quality is poor. They are noisy, blurry, and low-resolution. Furthermore, the thermal image contrast between oil and water is frequently so small that OSD becomes problematic and difficult. Finally, infrared (*IR*) cannot be used to measure slick thickness, in general, [8]. Polarimetric imaging, on the other hand, has distinct

advantages for a variety of detection and classification problems [32]. This sensor's light reflects directly from the surface, containing the most information on surface oil [17]. Even so, oil in the water has a polarizing effect on light, so viewing oiled water through polarized lenses may increase contrast and oil detection. Furthermore, while advancing specific signatures related to surface smoothness, orientation, and target composition [33], the polarization of backscattered light is preserved. Recently, the polarized patterns of some animals have influenced image formation within their visual fields. As a result, it is natural to adopt some of these behaviors in the world of computer vision for a variety of biologically inspired applications. Polarimetric technology can produce more accurate results on high-density-based oil spill segmentation and measurement cases than conventional thermal imaging, which can be used to classify the thickness of oil films. However, there is evidence that image quality is primarily determined by angles, which result in under-exposed and over-exposed illuminated regions. Tables I and II compare the advantages and disadvantages of thermal and polarimetric imagery sensors.

Image binarization is an important step in preprocessing, particularly for data analysis. Binarization is the process of converting grayscale or color images into two-tone images (black or white regions). Binarization, on the other hand, presents unique challenges that can take many forms. The most common tasks in remote sensing, however, are object detection and recognition, classification, and analysis. Binarization is used to: 1) separate the image into distinct regions containing each pixel with similar characteristics; and 2) segment the image. In practice, thresholding is one of the most basic and widely used image segmentation techniques. In image binarization, a threshold value is manually selected, and all pixels with values greater than the threshold are classified as white, while all other pixels are classified as black. The binarization process is difficult due to image noise and degradation. The problem is deciding on an appropriate image-driven threshold. Numerous studies have recently focused on binarization tools [18], [35].

D. Image Binarization

However, there is no agreement on the accuracy of the results because, in most cases, the sensors produce low-resolution

images that are primarily noisy or blurry. Mustafa et al. [39] discovered a method for evaluating the shortcomings of algorithms for degraded image binarization. The authors propose a new algorithm that will improve image binarization methods by employing a more reliable methodology. Furthermore, given the characteristics of the existing sensors, finding a perfect oil spill image binarization solution is more difficult. According to [39], available binarization methods can be classified into two broad categories: binarization based on global or single threshold and local binarization based on region.

1) *Global Threshold-Based Binarization (GTB)*: The goal of global threshold-based binarization (GTB) on the other hand is to find the global threshold for the entire image and binarize it using a single threshold. Using image-driven global characteristics parameters, a global binarization concept divides the image's entire dynamic range into two classes. For example, Otsu automatically determines the threshold value based on global and between-class variance [40]. Kapur et al. [41] proposed cross-entropy-based algorithms. However, when images, including thermal and polarimetric images, are contaminated with noise or poor quality, these methods do not guarantee the best threshold selection process because no spatial correlation is taken into account. The GTB methods can be used for a variety of image processing tasks, including image enhancement [42] and uniform-illuminated image segmentation. In general, global methods either lose or suppress the image's local variance, which may contain important information or content.

2) *Local Binarizations (LB)*: Class divides an image into regions where the local threshold is calculated, and then evaluates a single threshold using their local thresholds. Because of various types of local property, cutting-edge binarization methods work with small block tiles and local information. Interestingly, some studies show that noisy details in local blocks result in classifying regions. As shown in Table III, the LB methods can be applied to a wide range of practical image-processing applications. Niblack [43] observes the threshold value using information from the local standard deviation and mean. The metric includes thresholds based on local information for various target tiles, such as Feng's method [39], Bradley's method [44], Sauvola's method [45], Nick's method [46], and Mustafa's method [47]. KM et al. [48] recently pioneered multiscale local tiles by combining different local thresholds with weights. After that, Oulefki et al. [10] expanded Sauvola's local metric [45] to introduce the local threshold metrics for oil spill segmentation. The resulting regions were given various shapes based on the acceptable error of the regions and the distance between the center and the boundaries. Table III shows the main limitations of commonly used methods. This variety of approaches: 1) has used filters to reduce noise from the image, but the use of the guided filter (best edge-preserving filter) has not been found, which is a factor that can increase the accuracy of the available binarization methods; and 2) contrast enhancement is done either by traditional methods or not. More research on preprocessing is required and warrants further investigation.

III. PROPOSED METHOD

This section proposes a high-density oil spill segmentation framework based on thermal and polarimetric images using local threshold segmentation. The proposed framework's significant steps are: 1) region initialization by identifying the initial regions of the oil spill; and 2) oil spill segmentation by creating a multithreshold using the PSO method.

A. Region Initialization

We divide the segmentation framework into three major steps to identify the initial regions of the oil spill, followed by association operators. The operators provide information about the oil spill's segmented areas.

1) *Multithreshold Determination Using the Particle Swarm Optimization (PSO)*: In this section, we present the determination of threshold numbers using PSO for calculating a threshold constant. The PSO algorithm simply uses the objective function to evaluate the candidate number of thresholds. For each k th iteration, the position of the threshold (t) is denoted by x_t^k . Threshold (t) moves in the space according to its velocity (v_t^k). The position of each threshold is updated by

$$x_t^{k+1} = x_t^k + v_t^{k+1}. \quad (10)$$

Threshold position x_t^{k+1} is the updated version of the last local best position plus threshold's velocity. It is estimated by five acceleration parameters ($c_1, c_2, r_1, r_2, \omega$) of the last velocity and runs the optimization process and is updated using the following:

$$v_t^{k+1} = \omega v_t^k + c_1 r_1 (p_t^k - x_t^k) + c_2 r_2 (g_t^k - x_t^k) \quad (11)$$

where p_t^k and g_t^k represent the local best position and the global best position of the threshold (t) at the k^{th} iteration. The learning factors (c_1, c_2) control the local best position's relative impact and the global best part on a threshold's velocity. A small number of learning factors allow each threshold to move far away from already uncovered satisfactory locations. A large number of the learning factors stimulate a more intensive search of a location close to satisfactory locations. The social factors (r_1, r_2) ensure that the algorithm is randomly determined whereas r_1 and r_2 belong to $[0, 1]$. An inertia weight factor is represented by ω , which controls the search performance in both global and local positions. The small number of inertia weight increases the local search performance, and the large number encourages global search performance.

Algorithm 1 describes all the steps of the modified PSO search algorithm. It initializes the threshold (t) or multithreshold (t_n) position first, then runs the algorithm to find the global best threshold position. In each iteration, the local and global best vectors are updated to estimate the velocity vector of each threshold. This process is iteratively calculated until the stopping condition is found. In this article, we used the correlation number $C(I_{i,j}, J_{i,j})$ of a logarithmic image ($I_{i,j}$) and a threshold-segmented image ($J_{i,j}$). It can be calculated by

$$C(I_{i,j}, J_{i,j}) = \frac{1}{N-1} \frac{1}{M-1} \sum_{i=1}^N \sum_{j=1}^M \left(\frac{I_{i,j} - \mu_I}{\sigma_I} \right) \left(\frac{I_{i,j} - \mu_J}{\sigma_J} \right) \quad (12)$$

TABLE III
COMPARISON OF DIFFERENT LOCAL THRESHOLD SEGMENTATION METHODS

Method	Threshold Description	Parameter
Feng et al. [39]	$T_{i,j} = \mu_{i,j} (1 - \alpha) + 2\alpha (\mu_{i,j} - I_{max}) \left(\frac{\sigma_{i,j}}{R_s} \right) + 3\alpha I_{max} \quad (1)$ <p>$\mu_{i,j} = a$ local mean, $\sigma_{i,j} = a$ local standard deviation, $\alpha = a$ coefficient, $I_{max} = a$ minimum number of grayscale levels, $R_s =$ the dynamic range of grayscale standard deviation.</p>	Manually an input parameter and a window size
Bradlay et al. [44]	$T_{i,j} = \mu_{i,j} \left(1 - \frac{k}{100} \right) \quad (2)$ <p>$\mu_{i,j}$ is a local mean, and $k=a$ constant, by default $k=12$.</p> <p>Limitation: illumination problem</p>	Manually input parameters
Sauvola et al. [45]	$T_{i,j} = \mu_{i,j} \left(1 - k \left(1 - \frac{\sigma_{i,j}}{R} \right) \right) \quad (3)$ <p>$\mu_{i,j}$ is a local mean, $\sigma_{i,j} = a$ local standard deviation, $k = a$ constant, by default $k = 0.1$, and $R = a$ gray-scale level, by default $R = 128$ for an 8-bit image. Limitation: When the contrast between the foreground and the background is small, missing low-contrast objects, keeping textured text as it is, handling badly various object sizes, spatial object interference.</p>	Manually input parameters
Nick et al. [46]	$T_{i,j} = \mu_{i,j} + k \sqrt{\frac{(I_{i,j}^2 - \mu_{i,j}^2)}{N}} \quad (4)$ <p>$\mu_{i,j} = a$ local mean, $I_{i,j} =$ an image, $N =$ the size of an image, and $k = a$ constant, by default $k = -0.13$.</p> <p>Limitation: if the contrast is too small or the text is in thin pen stroke text.</p>	Manually input parameters
Mustafe et al. [47]	$T_{i,j} = \frac{\{x,y\} + \mu}{2} \left[1 - k \left(1 - \frac{\sigma_{i,j}}{R} \right) \right] \quad (5)$ <p>$\{x,y\} =$ the maximum intensity of an input image, $\mu = a$ global mean, $\sigma_{i,j} = a$ local standard deviation, $k = a$ constant, and $R = a$ gray-scale level, by default $R=128$ for an 8-bit image.</p>	Manually input parameters
Sos et al. [48]	$T_{i,j} = \gamma_1 \mu_{i,j} (1 + C\hat{\sigma}) + \gamma_2 \quad (6)$ $\hat{\sigma} = \tau I_{i,j} + \sigma_{i,j} (1 - \tau) \quad (7)$ <p>$\tau = a$ weight, γ_1 and $\gamma_2 =$ the intensity characteristics of an input image ($I_{i,j}$), $\mu_{i,j} = a$ local mean, $C = a$ constant, and $\sigma_{i,j} = a$ local SD.</p>	Manually input parameters
Oulefki et al. [10]	$T_{i,j} = \mu \left(1 - \frac{\sigma}{\alpha(L-1)} \right) \quad (8)$ <p>$\mu = a$ global mean luminance number, $\sigma = a$ global standard deviation number, $L =$ the total luminance level, and $\alpha = a$ constant.</p>	Manually input parameters
Proposed	$T_{i,j} = N_{i,j} \left(1 + s_{\Phi} \left(\frac{2\sqrt{N_{i,j} + mN_{i,j}^2 - 2N_{i,j}D_{i,j}}}{L(m-1)} - 1 \right) \right) \quad (9)$ <p>where $N_{i,j}$ represents a normalized image, s_{Φ} represents an optimal threshold constant, $D_{i,j}$ represents a denoised image, m represents the size of a multi-threshold, and L represents a grayscale level, by default $L=128$ for an 8-bit image.</p>	Automatic Image-Dependent Threshold

where μ_I and σ_I represent the mean and the standard deviation of a logarithmic image ($I_{i,j}$). μ_J and σ_J represent the mean and the standard deviation of a threshold-segmented image ($J_{i,j}$), respectively. N and M are the sizes of an image.

The threshold-segmentation method is one of the most common methods for the segmentation of images into bilevel or more levels. It is a simple and popular method in the digital image processing field. Bilevel threshold methods encourage binarization, and the result after segmentation is a binary image.

TABLE IV
POLARIMETRIC-BASED IMAGES CREATED BY THE SENSOR WITH THE SPECIFICATION [55]

Detector	Uncooled Vox Microbolometer array
Waveband (microns)	7.5–13.5
Pixel pitch (microns)	17
Resolution	400 × 300
Resolution	640 × 512
Frame rate (Hz)	7.5 or 30 Hz
Full frame pixel operability	99.9%
Image products	Radiance, S1, S2, DoLP, Orientation, ColorFuse, 14-bit raw
Sensitive material	Vanadium
Typical NETD (mK)	Less than 30
Power consumption (mW)	Less than 250
Weight (grams)	Less than 15
Operating temperature	−40°C ~ +85°C

Algorithm 1: Find the Number of Thresholds Using PSO.

Input: Initialize multi-threshold (t_n), inertia weight (ω), and stop condition $C(I_{i,j}, J_{i,j})$, learning factors (c_1, c_2), each threshold position and velocity randomly

Read an image ($X_{i,j}$)

- 1 Map the input image into a logarithmic domain, $I_{i,j} = \log(X_{i,j} + 1)$
- 2 **for** all threshold positions **do**
- 3 **for** all input training threshold sets **do**
- 4 Apply input training threshold sets to the input image
- Calculate the mean number of regions, separated by training threshold sets
- Replace the mean number into each separated region
- Calculate a correlation number $C(I_{i,j}, J_{i,j})$
- Update a correlation number
- 5 **if** Correlation number \geq Local best value **then**
- 6 Update a local best value and a local best vector
- 7 **else**
- 8 Increase the number of thresholds
- 9 **for** All threshold positions **do**
- 10 Update a global best to the maximum correlation number
- Update a global vector
- Update a threshold velocity vector
- Update a threshold position vector
- 11 Calculate the number of pixels in the separated regions ($I_{i,j} \leq t_n$ and $I_{i,j} > t_n$)
- 12 Calculate the threshold constant (s)

Multilevel threshold methods are a low-computational complexity. It is suitable for multilevel segmentation, but a major drawback is determining the number of thresholds. In this article, the number and position of thresholds are used to calculate a threshold constant. It can be used for local segmentation and will be described in the next subsection. For the calculation of a threshold-segmented image, it can be computed by

$$J_{i,j} = \begin{cases} \frac{1}{N_1} \sum_{i,j=1}^{N_1} I_{i,j}, 0 \leq I_{i,j} < t_1 \\ \frac{1}{N_2} \sum_{i,j=1}^{N_2} I_{i,j}, t_1 \leq I_{i,j} < t_2 \\ \dots, t_2 \leq I_{i,j} < t_n \\ \frac{1}{N_n} \sum_{i,j=1}^{N_n} I_{i,j}, t_n \leq I_{i,j} < L - 1 \end{cases} \quad (13)$$

where t_n represents the multilevel threshold position. L represents the total number of a permitted intensity range. N represents the total number of pixels in each multilevel threshold segmentation and $I_{(i,j)}$ denotes an input image.

2) *Calculation of an Optimal Threshold:* Binarization methods are commonly used for image segmentation. By a global threshold, the classical binarization method suffers from intricate details, which contain foreground details close to background details. Sauvola's binarization method [45] for document images has some advantages. It works well on noisy and blurry images. Also, it is low-computational. However, it suffers from several limitations like low-contrast, texture texts or regions, spatial object interference, for instance [45], [49]. In this subsection, we are considering the calculation of an optimal

Algorithm 2: The Initialization of Oil Spill Regions.

Input: Threshold-segmented image ($J_{i,j}$), optimal threshold constant (s_Φ), the size of the multilevel threshold (n)

13 Generate the size of a filter, $m = 2n + 1$.
 Generate a filter sizing $m - by - m$
 Generate a denoised image ($D_{i,j}$) by applying the filter to the segmented image ($J_{i,j}$)
 Generate a normalized image, $N_{i,j} = D_{i,j}/m^2$

14 **if** $s_\Phi \neq 0$ **then**
 15 \lfloor Calculate the local threshold metric ($T_{i,j}$) by using the optimal threshold constant (s_Φ)
 16 **else**
 17 \lfloor Define the local threshold metric, $T_{i,j} = N_{i,j}$

18 Generate initialized oil spill regions by binarizing the segmented image ($J_{i,j}$) with the local threshold metric ($T_{i,j}$)
Output: Initial oil spill region metric ($B_{i,j}$)

Algorithm 3: Oil Spill Segmentation.

Input: logarithmic image ($I_{i,j}$), initial oil spill region metric ($B_{i,j}$)

19 **Initialize:** Cost Function ($CF = 0$)
 Cardinality of Region, $R = \text{card}\{B_{i,j}\}$

20 **while** $CF < a \text{ set point } (k)$ **do**
 21 **while** $\mu_n < 1$ **do**
 22 Calculate $[N_{i,j}]_n = [N_{i,j}]_n + \alpha_{11}[N_{i-1,j-1}]_n + \alpha_{12}[N_{i-1,j}]_n + \dots + \alpha_{33}[N_{i+1,j+1}]_n$ where
 $\{N_{i,j}\} = \{N_{i,j} \in B_{i,j}, I_{i,j}\}$, n represents the order number of regions $B_{i,j}$, α
 represents a binary weight.
 23 Update a local mean (μ_n) of $[N_{i,j}]_n$
 Update n , $n=n+1$
 24 \lfloor Calculate a CF number

Output: Segmented image – oil spill regions, ($Y_{i,j}$)

threshold regarding thermal and polarimetric image segmentation.

Algorithm 1 describes the initialization of oil spill regions by using an optimal threshold. In each iteration n^{th} , the multilevel threshold is shifted to the next level threshold, then calculate the optimal threshold (S_Φ) until the stopping criteria ($S_\Phi > k$) are met in the end of a threshold (t_n). For the calculation of the optimal threshold, it can be written as

$$s = 1 - \frac{\text{card}\{I_{i,j} \mid I_{i,j} \leq t_n\}}{\text{card}\{I_{i,j} \mid I_{i,j} > t_n\}} \quad (14)$$

where $\text{card}\{\bullet\}$ represents a cardinality operator.

3) *Initialization of Oil Spill Regions:* In this section, we are defining initialized oil spill regions. The region initialization requires dividing the entire image into small tiles, then calculating a local threshold metric. In this case, the local threshold binarization method is suitable for the local region segmentation. However, it requires modifying some calculations for oil spill segmentation as shown in Algorithm 2.

Take note that (11) contains some Sauvola's parameters [45], [47], [49], if $N_{i,j}$ represents a mean number, s_Φ represents a user-defined constant, $L(m-1)$ represents a gray level constant, and $2(N_{i,j} + mN_{i,j}^2 - 2N_{i,j}D_{i,j})^{1/2}$ represents a standard deviation number. The local threshold metric is used to binarize a threshold-segmented image ($J_{i,j}$). Initial oil spill

regions ($B_{i,j}$) can be conditionally binarized as

$$B_{i,j} = \begin{cases} 1, & J_{i,j} > T_{i,j} \\ 0, & J_{i,j} \leq T_{i,j} \end{cases} \quad (15)$$

where $J_{i,j}$ represents a threshold-segmented image and $T_{i,j}$ represents a local threshold metric. The calculation of this is presented on the last line of Table III.

B. Oil Spill Segmentation

In this section, the approach to oil spill region segmentation considers the surrounding pixels of initial oil spill regions ($B_{i,j}$) and calculates the surrounding pixels. If those surrounding pixels contain an intensity close to initial oil spill regions, they can be added to the same region. For a technical description, it is described in Algorithm 3.

C. Cost Function (CF)

A cost function measures the accuracy of the segmented image compared with the ground truth. In this article, we proposed the segmentation framework for an oil spill application. It requires a special cost function. The segmentation optimization processes can stop processing when the accuracy is close to the ground

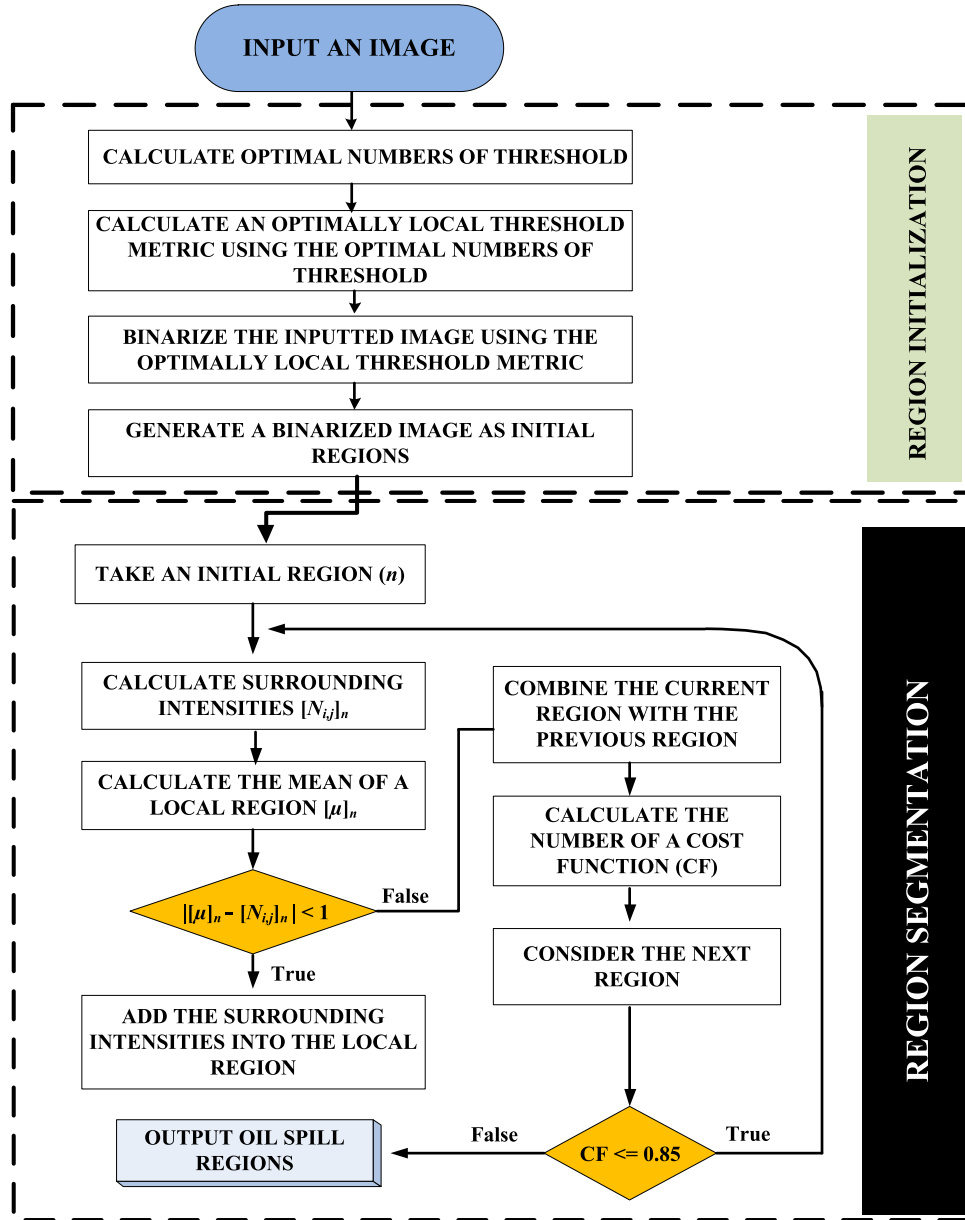


Fig. 2. Pipeline of the proposed oil spill detection.

truth [50]. The details of ground truth segmentation be found in [51].

Let $X_{i,j}$, $Y_{i,j}$, and $G_{i,j}$ be an original image, a segmented image, and ground truth, respectively. The cost function is intruded as the combination of the ratio of region size (ρ_A) and the ratio of region details (ρ_E). The cost function can be described as

$$CF = \frac{A_S}{A_G} \cdot \frac{E_S}{E_G} \quad (16)$$

where A_s and A_g , respectively, denote the size of segmented and ground truth regions; $A_s = \text{card}\{Y_{i,j} \mid \forall Y_{i,j} = 1\}$ and $A_G = \text{card}\{G_{i,j} \mid \forall G_{i,j} = 1\}$, E_s and E_G represent the enhancement value related to segmented and ground truth regions,

respectively. It can be calculated as

$$E_S = \sum_{i,j=1,1}^{M,N} \{EME_{i,j} \mid \forall Y_{i,j} = 1\} \quad (17)$$

$$EME_{i,j} = \frac{[I_{max}]_{i,j}^{m,n} - [I_{min}]_{i,j}^{m,n}}{[I_{max}]_{i,j}^{m,n} + [I_{min}]_{i,j}^{m,n}} \times \log \left(\frac{[I_{max}]_{i,j}^{m,n} - [I_{min}]_{i,j}^{m,n} + 1}{[I_{max}]_{i,j}^{m,n} + [I_{min}]_{i,j}^{m,n} + 1} \right) \quad (18)$$

where $[I_{max}]_{i,j}^{m,n}$ represents a local maximum intensity, $[I_{min}]_{i,j}^{m,n}$ represents a local minimum intensity, m and n represent the size of a local tile, i and j represent the pixel location of an original image, $\text{card}\{\bullet\}$ represents a cardinality operator,



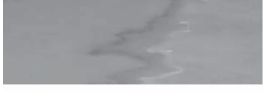

Data N°	Type of Images	Resolution in Pixels	Images N°	Equipment	Sample
1	Thermal	300 × 100	496	FLIR	
2	Thermal	300 × 100	383	FLIR	
3	Polarimetric	300 × 100	120	Polaris	
4	Polarimetric	300 × 100	100	Polaris	

Fig. 3. Data set description.

and $EME_{i,j}$ represents the enhancement metric by entropy [52], [53], [54]. To recap this section, Fig. 2 describes the methodology that has been developed. It gives insight into how the region segmentation is calculated and initiated.

IV. COMPUTER SIMULATION RESULTS

The experimental results of the proposed oil spill segmentation process are presented in this section. To begin, the proposed achieves cutting-edge results on an oil spill data set in both thermal and polarization-based imaging. Second, we show the 3-D visualization and the detected oil spill region. A

A. Data Set Descriptions and Algorithm Configurations

We have created four publicly available thermal and polarimetric oil spill image data sets [47]. Those data sets contain several hundred images captured by thermal and polarimetric sensors. The data sets descriptions are described in Fig. 3.

All experiments are conducted on an iMac with a 3.30-GHz Intel CPU, AMD Readon R9 M290 graphical processing unit (GPU), and 8 GB of RAM. We have set the learning factor of $c_1 = 2$ and $c_2 = 2$, the inertia weight of $\omega = 5$, and the set points in Algorithms (2 and 3) of $k = 0.90$ and $k = 0.85$, respectively. The constant numbers of compared methods were set independently, and the best results were selected for each method. The primary condition adapted was to see if the oil spill region was detected, and the cost function number was close to the ground truth. In the classical PSO algorithm, c_1 represents a cognitive constant, c_2 denotes a social constant, and ω refers to an inertial factor. These parameters are used as mainly controlling parameters. If c_1 is set as 0, the particle has no cognitive ability, if c_2 is set as 0, there are no shared details between particles. In contrast, a relatively high value of the social and cognitive components may lead particles to rush prematurely toward the optimal area. Much research has suggested setting either of the acceleration coefficients at 2 to make the mean of both stochastic factors. For the ω -parameter, if ω is set as 0, the velocity of a particle depends on its current position. If $\omega > 0$, the particle tends to explore new space. We have set $\omega = 5$

to reduce the time complexity in segmenting processes. The last parameter, κ , is set to exit the oil spill segmentation. If $\kappa = 0.85$, the segmentation performance must be more than 85%. Testing the proposed segmentation with the PSO algorithm trades off between the segmentation performance and time complexity. For $\kappa = 0.85 \sim 0.90$, the results can be illustrated in a while. The proposed qualitative performance (visual assessment), as shown in Fig. 5 outperforms the state-of-the-art segmentation methods.

B. Oil Spill Segmentation on Thermal and Polarimetric Data Sets

This section will begin by outlining a visually comparative evaluation, as shown in Fig. 4. The most advanced segmentation methods depict the oil spill regions, but the results are inaccurate and contain a lot of background noise. These methods perform poorly in separating considered oil spill regions. This is not the case with the proposed method; the proposed segmentation images include oil spill regions but no noisy background information. The oil spill zones are well-defined and separated. We will use the polarimetric images generated by the sensor described in [55]. Table IV presents a detailed specification of the polarimetric sensor used in this study, including the sensor's spatial resolution, operating frequency, and polarimetric mode.

1) *Multidensity Oil Spill Segmentation and 3-D Visualization*: According to the illustrative oil spill segmentation results in Fig. 5, all optimized regions can be reconstructed as multidensity segmented regions. Hence, we conducted the initialization by using the first slice S_1 . Thus, all-region numbers gradually grow based on the set point of an acceptable segmentation error. When the error increment, the optimization generates more and more slices until it reaches the set point. The last slice partially contains the lowest oil spill density region because its region error is close to its region set point. On the other hand, the first slice partially provides the highest oil spill density region due to its least region error.

The last column of Fig. 4 shows the average execution time. For the parameters used, each method's expected execution time is worse. In contrast, the proposed algorithm performs better, in terms of computational time. This proves that this new paradigm

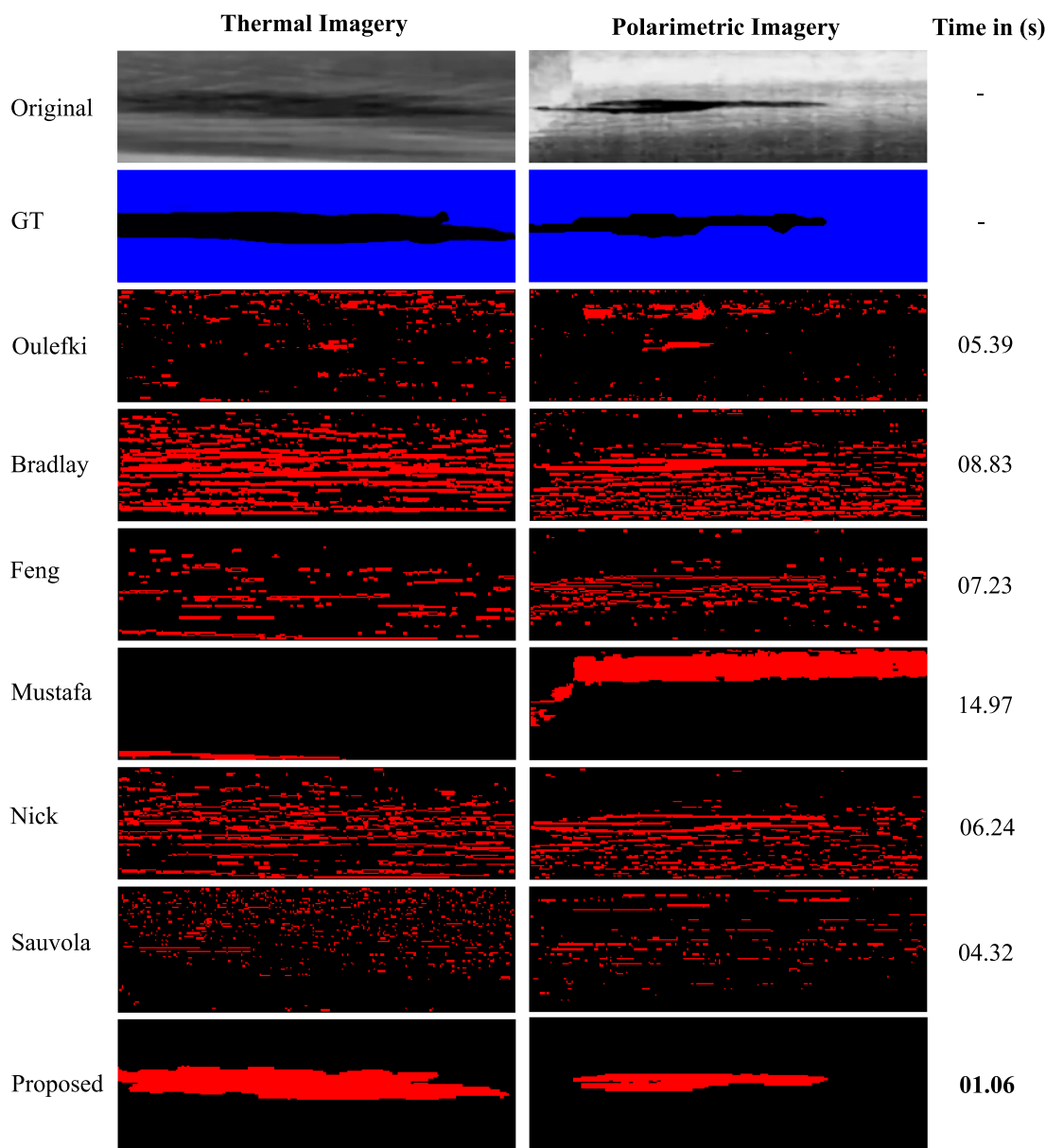


Fig. 4. Comparison of existing segmentation methods visually and by average execution time.

of spill detection is capable of a reduction of energy consumption and completion time.

Fig. 5 depicts a visual representation of the proposed results using thermal and polarimetric synthetic aperture radar (Pol-SAR) images. Because traditional thermal imagery depicts an oil spill based on reflected and emitted heat radiation, it is simple to reveal various oil spill densities on the water surface, as shown in Fig. 5. Another angle-based thermal image, known as polarimetric thermal imagery, depicted oil spill regions on grid polarizes and was aligned at 0° , 45° , 90° , and 135° and projected on a vertical and horizontal plane. Mathematical operations are used to complete the calculation of a Pol-SAR image. An image depicts vital regions with narrow visual luminance levels, but some details within radiated areas may be washed out. It trades off between region correction and region details. Therefore, using Pol-SAR imagery to generate a multidensity image is

more complicated than a classical thermal image, as presented in Fig. 5(b) Pol-SAR.

2) *Alternative Polarimetric Image (Thermal-to-Pseudopolarimetric)*: Increasing the local contrast of thermal images is another option for converting them to polarimetric images. It creates a strong boundary between regions while also emphasizing local details. It is an excellent choice for oil spill applications that require polarimetric imaging. This section employs remote sensing enhancement algorithms to convert thermal images into pseudopolarimetric images [56], [57].

Fig. 6 shows a comparison of a conventional thermal image and its enhanced image. The improved thermal image includes a critical edge feature, similar to a polarimetric image. The 3-D representation confirms the sharp distinction between oil and nonoil regions. It also provides local information for both oil spill and nonoil spill areas. Some low-density areas, however,

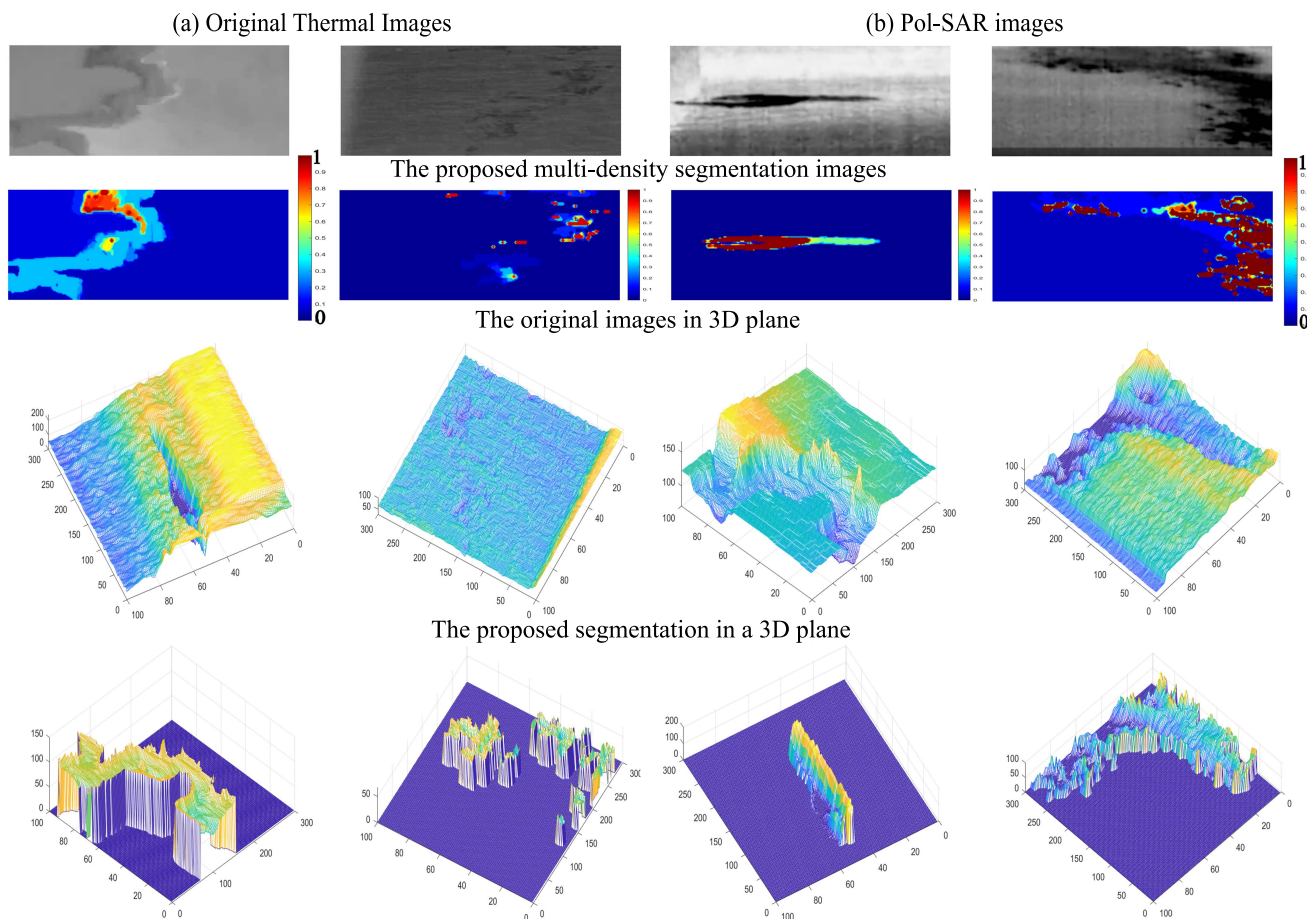


Fig. 5. Multidensity segmentation and 3-D visualization using the proposed segmentation on thermal and polarimetric images.

TABLE V
COMPARING THE PROPOSED SEGMENTATION PERFORMANCE WITH STATE-OF-THE-ART SEGMENTATION METHODS; THE BEST RESULTS HIGHLIGHTED WITH RED COLOR

Segmentation Methods	Quality metrics							
	Accuracy	Sensitivity	F-Measure	Precision	MCC	Dice	Jaccard	Specificity
Proposed	0.91	0.98	0.95	0.92	0.69	0.95	0.9	0.65
Oulefki [10]	0.78	0.15	0.21	0.83	0.14	0.21	0.14	0.91
Bradlay [44]	0.76	0.85	0.85	0.86	0.30	0.85	0.74	0.47
Feng [39]	0.76	0.93	0.86	0.81	0.05	0.86	0.76	0.09
Mustafe [47]	0.74	0.92	0.85	0.80	0.09	0.85	0.74	0.01
Nick [46]	0.74	0.87	0.84	0.83	0.12	0.84	0.73	0.21
Sauvola [45]	0.80	0.92	0.88	0.86	0.34	0.88	0.79	0.4

have been abandoned. The polarimetric alternatives reveal high-density oil spill regions.

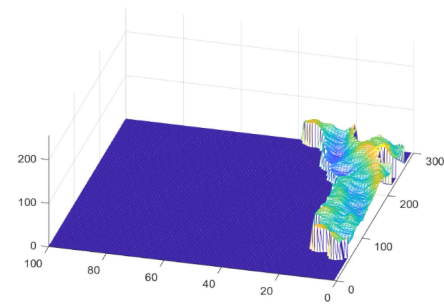
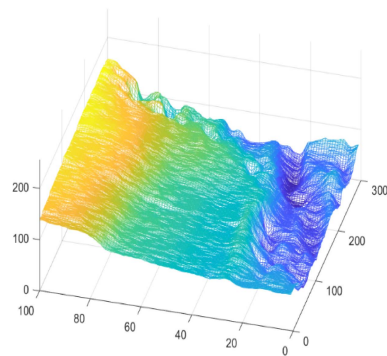
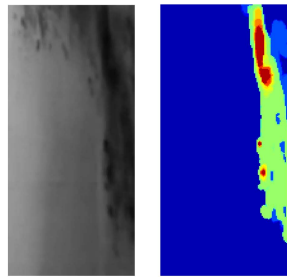
C. Quantitative Assessments

The comparison with relevant approaches would be unfair due to the lack of general approaches, as no current method approaches the oil spill segmentation in the same way. Nonetheless, we used the accuracy, sensitivity, F-measure (F-M), precision, specificity, MCC, Dice, and Jaccard to ensure that the model matched the data. More information on segmentation performance metrics is contained in [50]. In our case, Table V

compares the proposed methods against Oulefki [10], Feng [39], Bradlay [44], Sauvola [45], Nick [46], and Mustafe [47] over thermal and polarimetric imagery data sets. The table depicts the distribution probability of the data at various values.

The better the segmentation performance illustrates, the higher the values obtained for accuracy, sensitivity, F-Measure, precision, MCC, Dice, Jaccard, and specificity. Except for the accuracy and specificity metrics, where Oulefki segmentation approaches outperform the proposed one, the proposed approach provides higher values of sensitivity, F-measure, precision, MCC, Dice, and Jaccard metrics than state-of-the-art methods.

Original Thermal Images



Pseudo polarimetric imagery

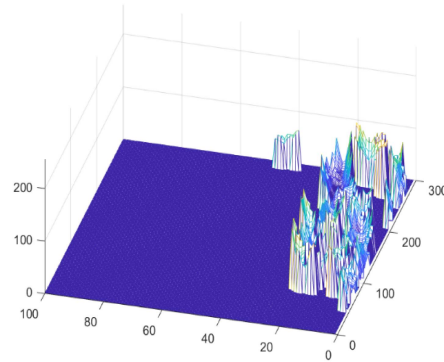
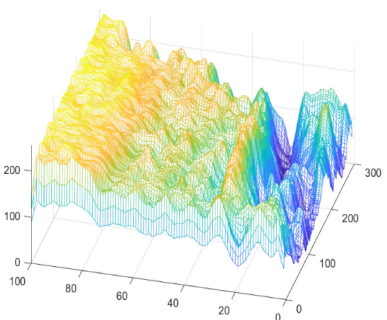
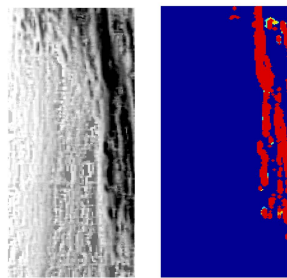


Fig. 6. Comparison of a thermal image with an enhanced thermal image: (first column) input images; (second column) multidensity representation; (third column) Inputted images in a 3-D plane; (fourth column) proposed segmentation in a 3-D plane.

V. CONCLUSION

Oil spill surveillance constitutes an essential component of oil spill disaster management since it can happen during oil transportation or storage and can be highly dangerous since wind, waves, and currents can scatter a large oil spill over a wide area within a few hours in the open sea. A study illustrated that 2475 spills released over 800 000 liters of oil in Toronto and surrounding regions between 1988 and 2000. This article introduced a new oil spill detection and visualization approach using thermal and polarimetric images for maritime applications. The application's novelty relies on: 1) the fact that the proposed method reveals oil spill regions while no human-provided parameters are initially required; 2) offering an efficient method for multilevel thresholding by using the minimum cross-entropy; 3) a nature-inspired optimized multithreshold segmentation framework with a 3-D visualization of the multidensity oil spill method; 4) creating an image drive-optimized enhancement algorithm applicable to both thermal and polarimetric images; and 5) offering simulation results for better understanding of the strengths and limitations of oil spill detection using thermal and polarimetric sensors images, which may help to improve the use of these sensors for protecting the environment and reducing economic losses and contingency planning. The proposed algorithm dramatically improves the detection of various types of weathered oil spills on the ocean surface, significantly advancing the current state of the practice with accuracy. The results show that the proposed solution could be used to detect oil films on the water surface. The proposed method illustrates the oil-spill detection performance. The effectiveness of the proposed oil

spill segmentation and visualization method was evaluated on two types of data—thermal and polarimetric data sets. The statistical assessment is determined using accuracy, sensitivity, F-measure, precision, specificity, Mathew correlation coefficient (MCC), Dice, and Jaccard, respectively: 0.91; 0.98; 0.95; 0.92; 0.69; 0.95; 0.9; 0.65. A long-term goal is to develop a day/night heat transfer model to determine oil spill thickness. We plan to propose an algorithm combining the developed method with the deep learning approach to classify various types of weathered oil spills efficiently. We believe that the developed model, combined with the presented method, may permit oil spill responders to measure oil spill thickness with existing, commercially available thermal radiometric cameras and has great potential for multiple applications in maritime surveillance.

REFERENCES

- [1] G. Levy, S. Vignudelli, and J. Gower, "Enabling earth observations in support of global, coastal, ocean, and climate change research and monitoring," *Int. J. Remote Sens.*, vol. 39, no. 13, pp. 4287–4292, 2018.
- [2] E. A. Karjadi, M. Badiey, J. T. Kirby, and C. Bayindir, "The effects of surface gravity waves on high-frequency acoustic propagation in shallow water," *IEEE J. Ocean. Eng.*, vol. 37, no. 1, pp. 112–121, Jan. 2012.
- [3] B. Liu, Y. Li, G. Li, and A. Liu, "A spectral feature based convolutional neural network for classification of sea surface oil spill," *ISPRS Int. J. Geo-Inf.*, vol. 8, no. 4, 2019, Art. no. 160.
- [4] Y. Lu, Q. Tian, X. Wang, G. Zheng, and X. Li, "Determining oil slick thickness using hyperspectral remote sensing in the Bohai Sea of China," *Int. J. Digit. Earth*, vol. 6, no. 1, pp. 76–93, 2013.
- [5] F. Nunziata, M. Migliaccio, and X. Li, "Sea oil slick observation using hybrid-polarity SAR architecture," *IEEE J. Ocean. Eng.*, vol. 40, no. 2, pp. 426–440, Apr. 2015.
- [6] C. Bayindir, J. D. Frost, and C. F. Barnes, "Assessment and enhancement of SAR noncoherent change detection of sea-surface oil spills," *IEEE J. Ocean. Eng.*, vol. 43, no. 1, pp. 211–220, Jan. 2018.

- [7] P. Ren, M. Xu, Y. Yu, F. Chen, X. Jiang, and E. Yang, "Energy minimization with one dot fuzzy initialization for marine oil spill segmentation," *IEEE J. Ocean. Eng.*, vol. 44, no. 4, pp. 1102–1115, Oct. 2019.
- [8] M. F. Fingas and C. E. Brown, "Review of oil spill remote sensing," *Spill Sci. Technol. Bull.*, vol. 4, no. 4, pp. 199–208, 1997.
- [9] J. Michel and M. Fingas, "Oil spills: Causes, consequences, prevention, and countermeasures," in *Fossil Fuels: Current Status and Future Directions*. Singapore: World Scientific, 2016, pp. 159–201.
- [10] A. Oulefki, T. Trongtirakul, S. Agaian, and W. Chiracharit, "Detection and visualization of oil spill using thermal images," in *Mobile Multimedia/Image Processing, Security, and Applications*, vol. 11399. Bellingham, WA, USA: SPIE, 2020, pp. 131–142.
- [11] M. Fingas and C. E. Brown, "Oil spill remote sensing: A review," in *Oil Spill Science and Technology*. Amsterdam, The Netherlands: Elsevier, 2011, pp. 111–169.
- [12] S. D. Jawak et al., "SIOS's earth observation (EO), remote sensing (RS), and operational activities in response to COVID-19," *Remote Sens.*, vol. 13, no. 4, 2021, Art. no. 712.
- [13] G. Guo, B. Liu, and C. Liu, "Thermal infrared spectral characteristics of bunker fuel oil to determine oil-film thickness and API," *J. Mar. Sci. Eng.*, vol. 8, no. 2, 2020, Art. no. 135.
- [14] J. Qi and D. S. Elson, "Mueller polarimetric imaging for surgical and diagnostic applications: A review," *J. Biophoton.*, vol. 10, no. 8, pp. 950–982, 2017.
- [15] T. Setälä, F. Nunziata, and A. T. Friberg, "Differences between partial polarizations in the space–time and space-frequency domains," *Opt. Lett.*, vol. 34, no. 19, pp. 2924–2926, 2009.
- [16] D. B. Chenault, J. P. Vaden, D. A. Mitchell, and E. D. DeMicco, "Infrared polarimetric sensing of oil on water," in *Remote Sensing of the Ocean, Sea Ice, Coastal Waters, and Large Water Regions*, vol. 9999. Bellingham, WA, USA: SPIE, 2016, Art. no. 99990D.
- [17] M. Migliaccio, F. Nunziata, and A. Buono, "SAR polarimetry for sea oil slick observation," *Int. J. Remote Sens.*, vol. 36, no. 12, pp. 3243–3273, 2015.
- [18] J. Xu, C. Cui, H. Feng, D. You, H. Wang, and B. Li, "Marine radar oil-spill monitoring through local adaptive thresholding," *Environ. Forensics*, vol. 20, no. 2, pp. 196–209, 2019.
- [19] M. Fingas and C. E. Brown, "A review of oil spill remote sensing," *Sensors*, vol. 18, no. 1, 2018, Art. no. 91.
- [20] K. Ren, Y. Lv, G. Gu, and Q. Chen, "Calculation method of multiangle polarization measurement for oil spill detection," *Appl. Opt.*, vol. 58, no. 12, pp. 3317–3324, 2019.
- [21] Y. Zhou, Y. Lu, Y. Shen, J. Ding, M. Zhang, and Z. Mao, "Polarized remote inversion of the refractive index of marine spilled oil from PARASOL images under sunglint," *IEEE Trans. Geosci. Remote Sens.*, vol. 58, no. 4, pp. 2710–2719, Apr. 2020.
- [22] I. Leifer et al., "State of the art satellite and airborne marine oil spill remote sensing: Application to the bp deepwater horizon oil spill," *Remote Sens. Environ.*, vol. 124, pp. 185–209, 2012.
- [23] D. Cantorna, C. Dafonte, A. Iglesias, and B. Arcay, "Oil spill segmentation in SAR images using convolutional neural networks. a comparative analysis with clustering and logistic regression algorithms," *Appl. Soft Comput.*, vol. 84, 2019, Art. no. 105716.
- [24] A. S. Solberg, G. Storvik, R. Solberg, and E. Volden, "Automatic detection of oil spills in ERS SAR images," *IEEE Trans. Geosci. Remote Sens.*, vol. 37, no. 4, pp. 1916–1924, Jul. 1999.
- [25] G. Li, Y. Li, Y. Hou, X. Wang, and L. Wang, "Marine oil slick detection using improved polarimetric feature parameters based on polarimetric synthetic aperture radar data," *Remote Sens.*, vol. 13, no. 9, 2021, Art. no. 1607.
- [26] M. Migliaccio, F. Nunziata, and A. Buono, "SAR polarimetry for effective sea oil slick observation," in *Proc. IEEE/OES Baltic Int. Symp.*, 2018, pp. 1–5.
- [27] F. Nunziata, A. Gambardella, and M. Migliaccio, "A unitary Mueller-based view of polarimetric SAR oil slick observation," *Int. J. Remote Sens.*, vol. 33, no. 20, pp. 6403–6425, 2012.
- [28] A. Pisano, F. Bignami, and R. Santoleri, "Oil spill detection in glint-contaminated near-infrared modis imagery," *Remote Sens.*, vol. 7, no. 1, pp. 1112–1134, 2015.
- [29] R. N. Clark et al., "A method for quantitative mapping of thick oil spills using imaging spectroscopy," US Department of the Interior, Geological Survey, 2010, pp. 1–51.
- [30] J. Jiao, Y. Lu, C. Hu, J. Shi, S. Sun, and Y. Liu, "Quantifying ocean surface oil thickness using thermal remote sensing," *Remote Sens. Environ.*, vol. 261, 2021, Art. no. 112513.
- [31] L. P. Osco et al., "A review on deep learning in UAV remote sensing," *Int. J. Appl. Earth Observ. Geoinf.*, vol. 102, 2021, Art. no. 102456.
- [32] H. Lang, J. Zhang, T. Zhang, D. Zhao, and J. Meng, "Hierarchical ship detection and recognition with high-resolution polarimetric synthetic aperture radar imagery," *J. Appl. Remote Sens.*, vol. 8, no. 1, 2014, Art. no. 083623.
- [33] G. C. Giakos, "Multifusion, multispectral, optical polarimetric imaging sensing principles," *IEEE Trans. Instrum. Meas.*, vol. 55, no. 5, pp. 1628–1633, Oct. 2006.
- [34] M. M. Espeseth, S. Skrunes, C. E. Jones, C. Brekke, B. Holt, and A. P. Doulgeris, "Analysis of evolving oil spills in full-polarimetric and hybrid-polarity SAR," *IEEE Trans. Geosci. Remote Sens.*, vol. 55, no. 7, pp. 4190–4210, Jul. 2017.
- [35] M. Muppidi, P. Rad, S. S. Agaian, and M. Jamshidi, "Image segmentation by multi-level thresholding using genetic algorithm with fuzzy entropy cost functions," in *Proc. Int. Conf. Image Process. Theory, Tools, Appl.*, 2015, pp. 143–148.
- [36] T. M. Alves, E. Kokinou, and G. Zodiatis, "A three-step model to assess shoreline and offshore susceptibility to oil spills: The South Aegean (Crete) as an analogue for confined marine basins," *Mar. Pollut. Bull.*, vol. 86, no. 1/2, pp. 443–457, 2014.
- [37] M. Migliaccio, A. Gambardella, and M. Tranfaglia, "SAR polarimetry to observe oil spills," *IEEE Trans. Geosci. Remote Sens.*, vol. 45, no. 2, pp. 506–511, Feb. 2007.
- [38] K. Panetta et al., "A comprehensive database for benchmarking imaging systems," *IEEE Trans. Pattern Anal. Mach. Intell.*, vol. 42, no. 3, pp. 509–520, Mar. 2020.
- [39] W. A. Mustafa, W. Khairunizam, Z. Ibrahim, A. Shahrman, and Z. M. Razlan, "Improved Feng binarization based on max-mean technique on document image," in *Proc. Int. Conf. Comput. Approach Smart Syst. Des. Appl.*, 2018, pp. 1–6.
- [40] M. Jin et al., "An automatic detection method of solar radio burst based on OTSU binarization," in *Proc. 11th Int. Conf. Digit. Image Process.* 2019, vol. 11179, Art. no. 111794C.
- [41] Z. Yan, J. Zhang, Z. Yang, and J. Tang, "Kapur's entropy for underwater multilevel thresholding image segmentation based on whale optimization algorithm," *IEEE Access*, vol. 9, pp. 41294–41319, 2021.
- [42] T. Trongtirakul, W. Chiracharit, and S. S. Agaian, "Single backlit image enhancement," *IEEE Access*, vol. 8, pp. 71940–71950, 2020.
- [43] B. Bataineh, S. N. H. S. Abdullah, and K. Omar, "An adaptive local binarization method for document images based on a novel thresholding method and dynamic windows," *Pattern Recognit. Lett.*, vol. 32, no. 14, pp. 1805–1813, 2011.
- [44] D. Bradley and G. Roth, "Adaptive thresholding using the integral image," *J. Graph. Tools*, vol. 12, no. 2, pp. 13–21, 2007.
- [45] X. Zheng, W. Tan, and J. Du, "A fast adaptive binarization method based on sub block OSTU and improved Sauvola," in *Proc. 7th Int. Conf. Wireless Commun., Netw. Mobile Comput.*, 2011, pp. 1–5.
- [46] K. Khurshid, I. Siddiqi, C. Faure, and N. Vincent, "Comparison of niblack inspired binarization methods for ancient documents," in *Proc. SPIE Document Recognit. Retrieval*, 2009, vol. 7247, Art. no. 72470U.
- [47] W. Mustafa, A. S. Abdul-Nasir, and Z. Mohamed, "Malaria parasites segmentation based on Sauvola algorithm modification," *Malaysian Appl. Biol.*, vol. 47, no. 2, pp. 71–76, 2018.
- [48] S. K. KM, R. Rajendran, K. Panetta, and S. Agaian, "A human visual based binarization technique for histological images," in *Proc. SPIE Mobile Multimedia/Image Process., Secur., Appl.* 2017, vol. 10221, Art. no. 102210Q.
- [49] Z. Hadjadj, A. Meziane, Y. Cherfa, M. Cheriet, and I. Setitra, "Isauvola: Improved Sauvola's algorithm for document image binarization," in *Proc. Int. Conf. Image Anal. Recognit.*, 2016, pp. 737–745.
- [50] A. Oulefki, S. Agaian, T. Trongtirakul, and A. K. Laouar, "Automatic COVID-19 lung infected region segmentation and measurement using CT-scans images," *Pattern Recognit.*, vol. 114, 2021, Art. no. 107747.
- [51] D. B. Chenault, J. Vaden, D. Mitchell, and E. Demicco, "New IR polarimeter for improved detection of oil on water," in *Proc. SPIE Newsroom*, 2018.
- [52] E. A. Silva, K. Panetta, and S. S. Agaian, "Quantifying image similarity using measure of enhancement by entropy," in *Proc. SPIE Mobile Multimedia/Image Process. Mil. Secur. Appl.* 2007, vol. 6579, Art. no. 65790U.
- [53] S. S. Agaian, "Visual morphology," in *Proc. SPIE Nonlinear Image Process.*, 1999, vol. 3646, pp. 139–150.
- [54] R. G. Kogan, S. S. Agaian, and K. P. Lentz, "Visualization using rational morphology and zonal magnitude reduction," in *Proc. SPIE Nonlinear Image Process.*, 1998, vol. 3304, pp. 153–163.
- [55] F. Yang and W. Shen, "Research on polarization detection technology of oil spill on sea surface," in *Proc. 7th Symp. Novel Photoelectron. Detection Technol. Appl.*, 2021, vol. 11763, pp. 1651–1660.

- [56] J. Betbeder, R. Fieuzal, Y. Philippets, L. Ferro-Famil, and F. Baup, "Contribution of multitemporal polarimetric synthetic aperture radar data for monitoring winter wheat and rapeseed crops," *J. Appl. Remote Sens.*, vol. 10, no. 2, 2016, Art. no. 026020.
- [57] S. Boutarfa, L. Bouchemakh, and Y. Smara, "Polarimetric synthetic aperture radar speckle filtering by multiscale edge detection," *J. Appl. Remote Sens.*, vol. 13, no. 2, 2019, Art. no. 024507.



Thaweesak Trongtirakul received the B.E. degree in electrical power engineering from the Rajamangala University of Technology Phra Nakhon (RMUTP), Bangkok, Thailand, in 2005, the M.Eng. degree in instrumentation engineering from the King Mongkut's Institute of Technology Ladkrabang (KMUTL), Bangkok, Thailand, in 2011, and the D.Eng. degree in electronics and telecommunication from King Mongkut's University of Technology Thonburi (KMUTT), Bangkok, Thailand, in 2020.

He is currently with the Electrical Engineering Department, Faculty of Industrial Education, RMUTP. Prior to his tenure with RMUTP, he was a Visiting Scientist with the College of Staten Island (CSI) and the Graduate Center, City University of New York (CUNY), New York, NY, USA. His research interests include the development of multimodel algorithms for simulation, signal processing, image processing, and video processing.



Sos Agaian (Fellow, IEEE) received the M.S. degree (*summa cum laude*) in mathematics and mechanics from Yerevan University, Yerevan, Armenia, the Ph.D. degree in math and physics from the Steklov Institute of Mathematics, Russian Academy of Sciences, Moscow, and the Doctor of Engineering Sciences degree from the Institute of the Control System, Russian Academy of Sciences. He is a Distinguished Professor of Computer Science with the Graduate Center/CSI, CUNY, New York, NY, USA. He was a Peter T. Flawn Professor with the University of Texas

at San Antonio, San Antonio, TX, USA. His research sponsors include DARPA, NSF, U.S. Department of Transportation, U.S. Department of Energy, NIJ, and private industry. His recent research interests include computational vision, artificial intelligence, multimedia security, multimedia analytics, and cancer screening.

Dr. Agaian is a highly cited scholar and ranked top one in image quality and multimedia analytics, assessed in 2022 by Google Scholar. Over 45 Ph.D. students have completed their Ph.D. thesis under his supervision. His work has led to over 750 articles, 10 books, 19 book chapters, and he holds over 56 American and foreign-issued or pending patents/disclosures. Several of his IP is commercially licensed. He is currently an Associate Editor of IEEE TRANSACTIONS ON IMAGE PROCESSING, IEEE TRANSACTIONS ON SYSTEMS, MAN, AND CYBERNETICS, and *Journal of Electronic Imaging (IS&T and SPIE): Systems*. He is a Fellow of the Society for Imaging Science and Technology (IS&T), Optical Society of America (SPIE), American Association for the Advancement of Science (AAAS), The Asia-Pacific Artificial Intelligence Association (AAIA), and a Foreign Member of the Armenian National Academy. He is a co-founder and served as an honorary/general cochair and/or committee member in many international conferences on image processing, computer vision, and AI. He received the Innovator of the Year Award in 2014 and the Tech Flash Titans-Top Researcher Award (San Antonio Business Journal). He gave more than 20 plenary/keynote speeches and 50+ Invited talks. He is the recipient of Influential Member of the School of Engineering, Tufts University, and a Certificate of Appreciation from the IEEE Educational Society, Central New England Council. Also, he has received several paper awards. He cofounded three Universities Centers: Simulation Visualization and Real-Time Prediction Center (NSF), NVIDIA Research Center, and the National Center of Academic Excellence in Cyber Defense (DHS). Presently, UTSA's cybersecurity program has been ranked the best in the nation.



Adel Oulefki received the Ph.D. degree in electrical engineering and computer science with honors from B.B.A University, El Anceur, Algeria, and academic research accreditation (HDR) degrees in electrical engineering from the Institute of Electrical Engineering and Electronics (IGEE), Boumerdes, Algeria in 2014 and 2018, respectively.

He has held various academic positions since 2016, such as Senior Researcher within the BIOSMC team, Centre de Développement des Technologies Avancées (CDTA), Baba Hassen, Algeria. In April 2018, he has been admitted for a position of MRA which primarily involved supervising the original research project. Prior to joining the CDTA, he has served as a temporary Assistant Lecturer with the Department of Electronics, B.B.A University from 2010 to 2014. His areas of expertise include signals, images, and video analysis, data clustering, pattern recognition using both RGB cameras and thermal sensors. His current research interests include interdisciplinary applications of computer science and engineering to the service of the security, environmental, medical, and agronomic areas.

Dr. Oulefki was awarded the prestigious scholarship (Fulbright) as a Visiting Scholar with the Department of Computer Science, College of Staten Island, CUNY, New York, NY, USA in September 2019.



Karen Panetta (Fellow, IEEE) received the B.S. degree in computer engineering from Boston University, Boston, MA, USA, and the M.S. and Ph.D. degrees in electrical engineering from Northeastern University, Boston, MA, USA, in 1985, 1988, and 1994, respectively.

She is currently the Dean of Graduate Engineering Education and a Professor with the Department of Electrical and Computer Engineering, Tufts University, Medford, MA, USA, where she is also an Adjunct Professor of Computer Science, and the Director of

Dr. Panetta's Vision and Sensing System Laboratory. Her research interests include developing efficient algorithms for simulation, modeling, signal, and image processing for biomedical and security applications.

Dr. Panetta was the recipient of the 2012 IEEE Ethical Practices Award and the Harriet B. Rigas Award for Outstanding Educator. In 2011, she was awarded the Presidential Award for Engineering and Science Education and Mentoring by the U.S. President Barack Obama. She is the Vice President of SMC, Membership, and Student Activities. She was the President of the 2019 IEEE-HKN. She is the Editor-in-Chief of *IEEE Women in Engineering Magazine*. She was the IEEE-USA Vice-President of communications and public affairs. From 2007 to 2009, she served as the Worldwide Director for the IEEE Women in Engineering, overseeing the world's largest professional organization supporting women in engineering and science.